REMOTE CHARACTERIZATION OF CHEMICAL VAPOR PLUMES BY LWIR IMAGING FABRY-PEROT SPECTROMETRY

Christopher M. Gittins and William J. Marinelli and James O. Jensen
Physical Sciences Inc.

Presented at:

		Form Approved OMB No. 0704-0188

Report Documentation Page

1. REPORT DATE **2001**	2. REPORT TYPE	3. DATES COVERED **00-00-2001 to 00-00-2001**

4. TITLE AND SUBTITLE **Remote Characterization of Chemical Vapor Plumes by LWIR Imaging Fabry-Perot Spectrometry**	5a. CONTRACT NUMBER
	5b. GRANT NUMBER
	5c. PROGRAM ELEMENT NUMBER
6. AUTHOR(S)	5d. PROJECT NUMBER
	5e. TASK NUMBER
	5f. WORK UNIT NUMBER

7. PERFORMING ORGANIZATION NAME(S) AND ADDRESS(ES) **Physical Sciences Inc,20 New England Business Center,Andover,MA,01810**	8. PERFORMING ORGANIZATION REPORT NUMBER

9. SPONSORING/MONITORING AGENCY NAME(S) AND ADDRESS(ES)	10. SPONSOR/MONITOR'S ACRONYM(S)
	11. SPONSOR/MONITOR'S REPORT NUMBER(S)

12. DISTRIBUTION/AVAILABILITY STATEMENT **Approved for public release; distribution unlimited**

13. SUPPLEMENTARY NOTES **The original document contains color images.**

14. ABSTRACT **see report**

15. SUBJECT TERMS

16. SECURITY CLASSIFICATION OF:			17. LIMITATION OF ABSTRACT	18. NUMBER OF PAGES **14**	19a. NAME OF RESPONSIBLE PERSON
a. REPORT **unclassified**	b. ABSTRACT **unclassified**	c. THIS PAGE **unclassified**			

Standard Form 298 (Rev. 8-98)
Prescribed by ANSI Std Z39-18

REMOTE CHARACTERIZATION OF CHEMICAL VAPOR PLUMES
BY LWIR IMAGING FABRY-PEROT SPECTROMETRY

Christopher M. Gittins and William J. Marinelli
Physical Sciences Inc.
20 New England Business Center, Andover, MA 01810-1077
e-mail: gittins@psicorp.com

James O. Jensen
U.S. Army SBCCOM
Edgewood Chemical and Biological Center
Aberdeen Proving Ground, MD

ABSTRACT

Physical Sciences Inc. has developed and tested two long-wavelength infrared (LWIR) hyperspectral imaging spectroradiometers based on the insertion of a rapidly tunable Fabry-Perot etalon in the field of view of a HgCdTe focal plane array (FPA). The tunable etalon-based optical system enables a wide field-of-view and the acquisition of narrowband (7 to 11 cm^{-1} spectral resolution), radiometrically calibrated imagery throughout the 8 to 11 μm spectral region. The instruments function as chemical imaging sensors by comparing the spectrum of each pixel in the scene with reference spectra of target chemical species. We present results of recent field tests in this paper.

INTRODUCTION

In this paper we describe the results of chemical imaging experiments involving two LWIR imaging Fabry-Perot spectrometers developed by Physical Sciences Inc. (PSI). (The instruments are known as Adaptive InfraRed Imaging Spectroradiometers, *AIRIS*™, U.S. Patent 5,461,477.) The experiments involved imaging a series controlled chemical vapor releases at the U.S. Department of Energy's Nevada Test Site. Plumes were viewed from two fixed locations: 1.5 km and 1.9 km range from the plume release point. We present data acquired during the summers of 2000 and 2001.

Passive sensing of chemical vapor plumes requires exploitation of both the spectral signatures of the target species as well as the radiance contrast between the vapor and the background scene. PSI's imaging spectrometers are comprised of an LWIR focal plane array-based camera which views the far field through a low-order, tunable Fabry-Perot etalon.[1,2] The tunable etalon provides the spectral resolution necessary to resolve structured absorption and emission from molecular vapors. The focal plane array (FPA) enables radiance measurements of sufficient accuracy that chemical vapors may be selectively detected with only several degrees effective temperature difference between the vapor and the background.

We analyze chemical imaging data using algorithms developed at PSI. The results of the data analysis illustrate two key sensor capabilities:

- Selective detection of one and two chemical species in plumes containing multiple species
- Detection of a single species with low false alarm rate using a limited number of detection bands.

Both of these capabilities have been demonstrated previously.[1] We have exercised a modified Gaussian plume dispersion model in conjunction with a multi-layer radiative transfer model to predict plume spectral signatures as a function of range downwind of their release point. The model predictions, which utilize local meteorological data as input, are in excellent agreement with the data. The ability to detect chemical plumes using AIRIS is not limited by instrument noise but by spectral clutter in the background scene against which the vapor plumes are viewed. (Instrument noise is a factor of 2-3 less than clutter noise.) This paper highlights our observations of plumes in absorption against a terrestrial background and our use of two AIRIS units to determine stand-off distance from the plume. The results of our passive ranging experiments reveal that we are able to determine range-to-target to ±5% accuracy, consistent with the uncertainty in the inputs to our triangulation calculation.

INSTRUMENT

A schematic illustration of the complete AIRIS optical train is depicted in Figure 1. The sensor design was developed by PSI and is described in prior publications.[1-3] The entire optical train is housed in a temperature regulated, sealed enclosure. The enclosure dimensions are ~70 x 30 x 30 cm. An integrated solid state air conditioner provides cooling of the enclosure interior.
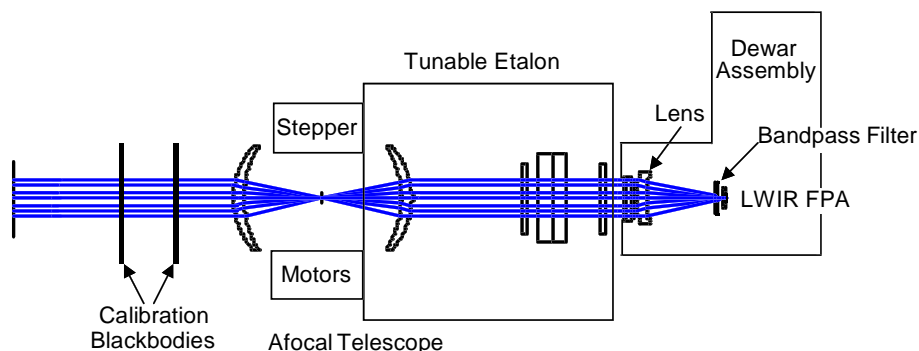

Figure 1. Schematic illustration of AIRIS optical train.

The Fabry-Perot interferometer (etalon) enables the sensors' hyperspectral capabilities. It operates as a tunable interference filter which selects the wavelength that illuminates the FPA. This configuration affords both wide field-of-view and broad spectral coverage. A bandpass filter is placed in front of the FPA to limit its response to a single etalon transmission order. Figure 2 depicts measured etalon transmission and spectral resolution (FWHM) over the etalon's operating range. There are ~40 spectral resolution elements over the interferometer's operating range. Although the second order (m=2) fringe may be continuously scanned to provide coverage of the 8 to 11 μm region, we have found that combined operation in m=3 (8 to ~10 μm) and m=2 (~10 to 11 μm) provides a better trade-off between spectral resolution and optical throughput for the chemical imaging applications we've investigated to date. The spacing and alignment of the etalon mirrors controlled via a closed-loop control system. The etalon can be tuned between resolution elements in 20 to 30 ms while maintaining wavelength positioning accuracy of ~1 cm^{-1}. The AIRIS system control program is derived from the software used to control the instrument's LWIR camera. Etalon control is accomplished within the system control program. Each AIRIS system computer is an Intel Pentium-based PC with Windows NT 4.0 as the operating system.
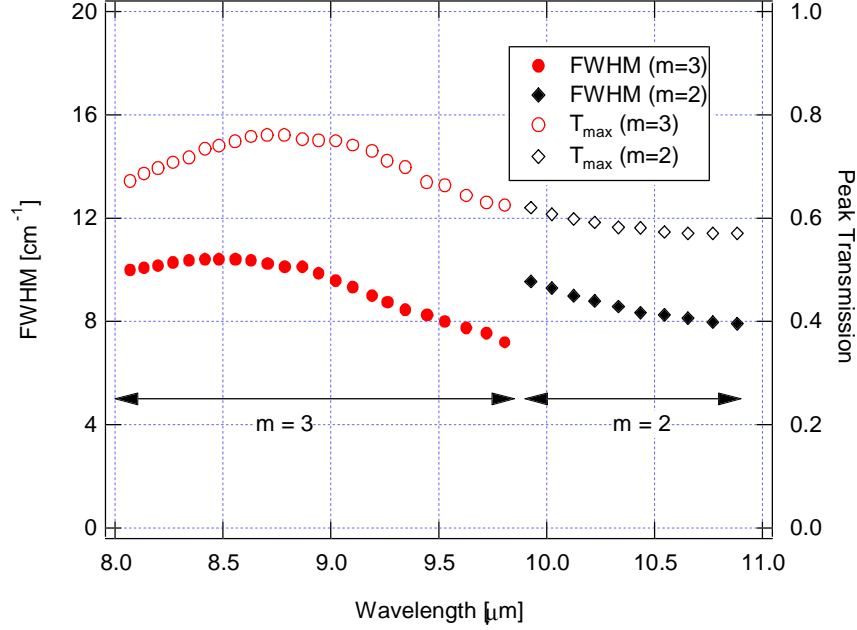
Figure 2. Peak etalon fringe transmission and FWHM as a function of wavelength; m=3 fringe from 8.0 to 9.8 µm and m=2 fringe from 9.9 to 10.9 µm.

The two sensors used to acquire data discussed in this work are identical except for their LWIR cameras. One sensor utilizes a 64 x 64 element HgCdTe FPA-based camera (SE-IR Corp., Goleta CA) and the second implements a 256 x 256 element HgCdTe FPA-based camera (Santa Barbara Focalplane, Goleta CA). Table 1 lists the salient characteristics of each instrument's camera and optical train.

TABLE 1. AIRIS-CW Characteristics

Property \ Instrument	64 x 64 FPA-based	256 x 256 FPA-based
Pixel pitch [µm]	61	40
Afocal telescope magnification	3:2	3:2
IFOV [mrad]	0.80	0.53
Field-of-regard [deg x deg]	3.0 x 3.0	7.8 x 7.8
FPA readout	rolling	snapshot
Camera frame rate [Hz]	21.3	114.9
FPA integration time [ms (typ.)]	1.44	0.56
A/D dynamic range [bits]	14	14

The 50 mm Ge lens located in front of the FPA results in an f/2.4 optical train. The lens provides diffraction limited focal spot size (~1 pixel) on-axis and ~2 pixels blurring (astigmatism) at the corners of the 64 x 64 pixel FPA. The imaging quality is high over the central ~200 x 200 pixels of the larger FPA, however the r.m.s. blur spot diameter is ~7 pixels at its corners. The 3:2 afocal telescope located beyond the tunable etalon module provides a fine adjustment of the system focus. (The 64 x 64 pixel AIRIS utilized a 1:1 afocal telescope prior to the 2001 field tests.) Two calibration blackbodies are mounted on a rotation stage and enable collection of radiometric calibration data. The high temperature blackbody is normally operated 10 to 15 K above ambient temperature and the low temperature blackbody operated ~5 K below ambient. The blackbodies are used to generate two point radiometric calibrations (gain and offset) for each pixel at each wavelength viewed. The calibration blackbodies are rotated clear of the system field-of-view during normal operation.

3

The figure-of-merit for a spectroradiometer is its noise equivalent spectral radiance (NESR). In an ideal instrument, the NESR is equal to the shot noise associated with photon arrival statistics. The observed NESR of the 64 x 64 element AIRIS is reaches a minimum of 1.0 µW/(cm^2 sr µm) at ~8.8 µm and increases to 1.3 and 2.4 µW/(cm^2 sr µm) at 7.9 and 10.9 µm, respectively. These values are characteristic of the A/D read-out noise of the LWIR camera, which is ~2x greater than calculated shot noise limited NESR.[1] We have not made precise measurements of the 256 x 256 element AIRIS's NESR. A preliminary evaluation of the data suggests its NESR is ~1-2x greater than the 64 x 64 element AIRIS's. This implies that the larger format AIRIS's NESR is also ~2x greater than calculated shot noise limit given the difference in integration times of the two sensors.

CHEMICAL DETECTION EXPERIMENTS

PLUME OBSERVATION CONDITIONS

The 64 x 64 element AIRIS has collected data during controlled chemical vapor releases at the U.S. Department of Energy's Nevada Test Site during the summers of 1999, 2000, and 2001. The 256 x 256 AIRIS was constructed in spring 2001 and operated during the 2001 field tests only. In this paper we present analyses of 1,1,1-trichloroethane (TCA), n-butanol, and dimethyl methylphosphonate (DMMP) releases from the 2000 and 2001 test series.

All chemical plumes were released from a 0.5 m diameter chimney orifice at ~10 m above ground level. A visible image of the plume release area viewed from 0.5 km stand-off is depicted in Figure 3. The wind direction during plume releases was extremely consistent from day-to-day. With respect to Figure 3, it blows from right to left. The chimney from which releases occurred can be seen at the right center of the image. Several low buildings are evident on either side of the chimney. The foreground is compacted sand. The background is a mountainside consisting of sand, rocks, and some low vegetation. Table 2 lists the stand-off range spatial resolution of each AIRIS at the plume release point during the 2000 and 2001 field tests. In all viewing configurations the stack diameter is less than the pixel size.

The TCA and n-butanol plumes were released from the stack at ~110°C; DMMP plumes were released at ~170°C. The plumes cooled and diluted as they propagated downwind. We present a quantitative analysis of plume cooling and dilution later in this section. The cooling and dilution rates are critically dependent upon the local wind speed/turbulence level. The wind speed was typically 6 to 10 m/s during releases, but was as low as several m/s and at times >15 m/s.
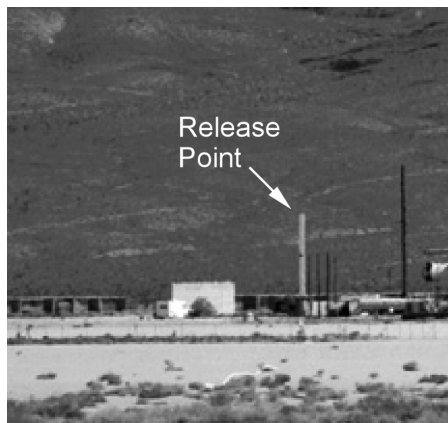

Figure 3. Visible image of the plume release area as viewed from 0.5 km stand-off. The chimney from which releases occurred can be seen at the right center of the image.

TABLE 2. Sensor Operating Ranges and Spatial Resolution at Range

	64 x 64 AIRIS	256 x 256 AIRIS
Summer 2000		
Range [km] / Resolution [m]	1.53 / 1.8	-
Summer 2001		
Range [km] / Resolution [m]	1.53 / 1.2	1.53 / 0.8
Range [km] / Resolution [m]	1.90 / 1.5	-

DETECTION APPROACH

The hyperspectral data cubes generated using AIRIS consisted of 36 narrowband images: 1260 cm^{-1} (7.94 µm) to 910 cm^{-1} (10.99 µm) in 10 cm^{-1} increments with the 64 x 64 system in 2000; 1270 cm^{-1} (7.87 µm) to 920 cm^{-1} (10.87 µm) in 10 cm^{-1} increments with both systems in 2001. Only 31 or 32 bands from 8.0 to 10.5 µm were used in most analyses. There were four objectives in the analyzing AIRIS data:

1. Demonstrate robust detection one or two species in the presence of multiple (potential interferent) species.

2. Maximize chemical detection sensitivity.

3. Minimize the false alarm rate, i.e., false positive detections of targeted chemical species.

4. Conduct rapid analysis of imagery. Ideally, imagery should be analyzed in real time, rather than in post processing.

To accomplish these objectives, we developed our own data analysis algorithms which were subsequently coded into IDL (RSI, Boulder CO). The detection algorithm searches for absorption and emission signatures characteristic of the target species. Absorption and emission signatures are inferred based on a statistical estimate of the background spectral radiance. The statistical based on the spatial variation of the spectral radiance within the scene. For the case of a single chemical species in an optically thin plume, the differential radiance at the sensor with and without the plume present is:

$$\Delta N(\lambda)_{sens} = N_{plume}(\lambda) - N_{bkgd}(\lambda) \approx \sigma(\lambda) \cdot \rho L \cdot \left[\frac{dN}{dT}\right]_{T_{bkgd}} \cdot \Delta T \qquad (1)$$

where σ is the chemical's absorption coefficient, ρL is its column density, the quantity in brackets is the derivative of the Planck function with respect to temperature (~16 µW/(cm^2 sr µm K) at 10 µm and 300 K), and ΔT is the effective temperature differential between the plume and the background. Our plume detection algorithm consists of four steps:

1. Perform a statistical estimate of $N_{bkgd}(\lambda)$ using the hyperspectral data set.

2. Subtract the estimated background from the data.

3. Determine the correlation between the differential radiance spectrum and the reference spectrum (spectra) of the species in the plume.

4. Mark pixels in the image which meet the user defined correlation criteria.

5

Background estimation is accomplished via a multi-band correlation analysis. (The 256 x 256 imagery was broken into 64 x 64 pixel subimages in this process.) Following Eq. (1), the differential radiance derived from hyperspectral data may be described in terms of basis spectra:

$$\Delta N_{sens}(\lambda) = \left[\sum_{i=1}^{n} k_i \cdot \sigma_i(\lambda) \right] + \delta(\lambda) = \Delta N_{calc}(\lambda) + \delta(\lambda) \tag{2}$$

where n is the number of basis spectra, the quantities k_i are fit coefficients which minimize the magnitude of δ, the fit residual. In all of our analyses n=1 or 2. The quantities ΔN_{sens} and ΔN_{calc} may be treated as vectors whose dimension is equal to the number of bands in the data analysis; the value of each element in the vectors is equal to differential radiance at λ_i. We define the correlation between the pixel spectrum

$$\chi = \frac{\overleftarrow{\Delta N}_{sens}}{\left| \overleftarrow{\Delta N}_{sens} \right|} \cdot \frac{\overleftarrow{\Delta N}_{calc}}{\left| \overleftarrow{\Delta N}_{calc} \right|} \tag{3}$$

We identify pixels where the maximum value of $|\Delta N_{calc}| \geq 12 \ \mu W/(cm^2 \ sr \ \mu m)$ and $|\chi| \geq 0.90$ as containing the target species. (Reducing the radiance or correlation thresholds generally increases the detection probability, but also usually lowers the ratio of positive detects to false alarms.) The IDL program which implements our plume detection approach processes a 64 x 64 x 31 hyperspectral data cube in ~10 seconds on a desktop PC (Pentium II, 256 MB RAM). The processing time scales linearly with the number of pixels in the array. The processed hyperspectral data cube is displayed to the user as a grayscale, synthetic broadband IR image with false color overlay showing the location of the detected plume. (The synthetic broadband IR image is created simply by summing the narrowband images.)

PLUME VISUALIZATION

Figure 4 depicts a DMMP release observed from 1.5 km stand-off using the 64 x 64 AIRIS. The pixels showing correlation with the DMMP reference spectrum are outlined in white. The DMMP concentration was 1800 ppmv at the release point and the release temperature was 170°C. The wind is blowing right to left in the scene. As expected, the plume is observed extending to the left of the release point. The DMMP plume is observed both in emission and absorption. It is observed in emission near the stack exit and in absorption further downwind. The differential radiance observed at the sensor is a function of the plume's optical density, $\sigma\rho L$ from Eq. (1), and the effective temperature differential between the plume and the background. Near the release point, the DMMP optical density (OD) is high, OD~1 at 9.5 μm, and the temperature differential is driven by plume temperature. The plume temperature comes into equilibrium with the air temperature fairly rapidly as the plume expands and propagates downwind. (A quantitative analysis of plume cooling and dilution is presented below.) Qualitatively, and with respect to Eq. (1), ΔT rapidly approaches a "steady state" value as the plume propagates downwind. In contrast to ΔT, the plume OD decreases as the plume spreads vertically but not as it spreads horizontally. Vertical plume spread is a strong function of atmospheric turbulence, which in turn is a strong function of wind speed. During most releases, the plume diluted to the point where its OD was too low for it to be detected against the "steady state" ΔT with the background. Because the winds were light during the release shown in Figure 4, the plume remained spatially coherent and its OD was high enough downwind that it could be observed against the effective temperature differential between the air and the background.
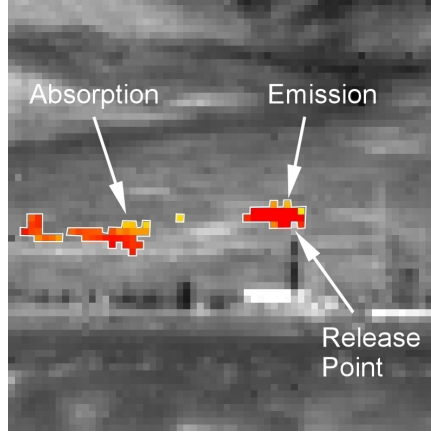
Figure 4. Synthetic broadband IR image of the plume release area. Pixels outlined in white indicate the location of the DMMP plume during a 1800 ppmv DMMP release. The plume is observed in emission near the release point and in absorption against the background further downwind.

Figures 5 and 6 depict differential spectra derived from the data at pixels in regions labeled "emission" and "absorption" in Figure 4. Also shown in Figure 5 and 6 are the best fits to the data using Eq. (4) with the known DMMP absorption spectrum. The observed differential radiance in Figure 6 would correspond to an effective temperature differential of 1.0 K for an optically thick plume. (We have no direct measurement of plume OD downwind of the release point.) FTIR measurements of the effective background temperature in this viewing geometry indicate that it is a strong function of solar illumination (time-of-day) and <8 K greater than the air temperature.[4] Simulations using MODTRAN indicate that the atmospheric transmission between the release point and the background is ~40% between 8 and 11 µm, i.e., a 20 K thermodynamic temperature differential between the air and the background corresponds to a 8 K effective temperature differential in Eq. (1). The fit residuals seen in Figures 5 and 6 are greater than the measured NESR of the instrument. We believe the observed residuals are attributable primarily to spectral clutter in the background scene. We believe spectral clutter is the fundamental limiting factor in our plume detection approach.
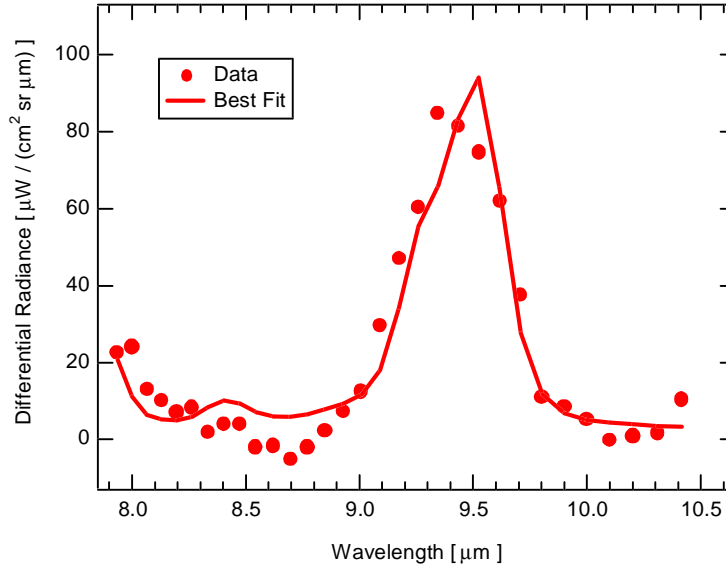

Figure 5. Recovered differential radiance spectra of one of the highlighted pixels from the region labeled "emission" in Figure 5; filled circles = data, solid line = best fit reference spectrum using Eq. (2).
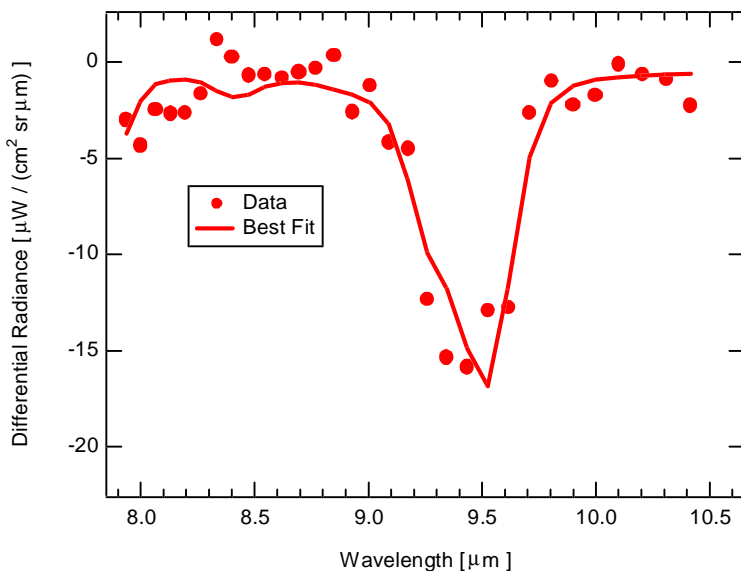
7

Figure 6. Recovered differential radiance spectra of one of the highlighted pixels from the region labeled "absorption" in Figure 5; filled circles = data, solid line = best fit reference spectrum using Eq. (2)

QUANTITATIVE ANALYSIS OF PLUME SIGNATURES

We have performed quantitative analyses of plume radiance levels as a function of distance downwind of the release point. We model plume signature as a function of downwind range by coupling standard models for mass transport and radiative transfer. Mass transport was calculated using a modified Gaussian plume dispersion model.[5] (The model was modified to obey conservation of mass at the release point.) Radiative transfer is calculated using a multi-layer atmospheric model.[6] Total radiance is calculated along the sensor's line-of-sight from the background to the sensor. Plume was calculated on a 10 cm grid for 5 m on either side of the propagation axis. (Under typical release conditions, the characteristic plume spread is ~4 m total 10 m downwind of the release point.)

Integration on the 10 cm grid accounts for the fact that the temperature gradient is severe and that plumes may not be optically thin in the immediate vicinity of the release point. The transmission between the sensor and plume was calculated using MODTRAN with a desert, summer model atmosphere. Figure 7 depicts the experimentally determined differential radiance at 9.17 μm, the peak of the TCA emission spectrum, as a function of distance downwind of the plume release point for several 1000 ppmv TCA releases. Also shown in Figure 7 are the calculated radiance levels at the sensor for Pasquill Class B (moderately unstable) and Class C (slightly unstable) atmospheric turbulence.[5] The average wind speed around the time of the measurement, 7 m/s, was also used to calculate plume radiance levels. Although the models do not accurately predict the radiance at the release point, the simulations with Class B and Class C model atmospheres do bracket the observed downwind data nicely. The same behavior was observed for species other than TCA. In practice, the target chemical species can be detected with low false alarm rate when the signal-to-clutter ratio at the peak emission (absorption) wavelength is at least 5:1; peak differential radiance ~12 μW/(cm^2 sr μm) under the observation conditions at NTS. The plume may be detected at lower signal-to-clutter ratios, but with an increased false alarm rate in the rest of the scene.
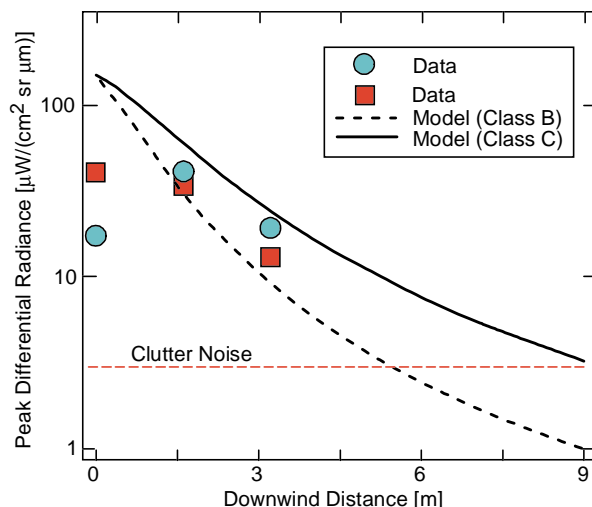
Figure 7. Calculated and experimentally determined differential radiance at 9.17 µm as a function of distance downwind of the plume release point for two 1000 ppmv TCA releases.

SELECTIVE DETECTION OF CHEMICAL SPECIES

We have investigated detection probability and false alarm rate as function of number of detection bands for single species releases.[1] Our analyses have focussed on DMMP and TCA releases. The analyses produced two key results:

- Detection probability does not increase with the number of bands when >5 bands are used in the analysis.

- The probability of false detection decreases rapidly up to ~7 detection bands, but only modest is achieved by including additional bands.

The reason that the detection probability does not increase with the number of bands used is that not every band in the spectrum contains useful information for identifying the target species. In fact, for most of the releases analyzed, increasing the number of bands beyond ~5 actually *lowered* the detection probability. This is because the additional bands did not provide additional identifying spectral information but did contain noise. The additional noise degrades the calculated correlation between the calculated differential radiance and the reference spectrum.

In addition to studying detection probability and false alarm rate for single species using reduced data sets, we have examined our ability to perform selective detection of target chemical species during multi-chemical releases and the susceptibility our detection approach to interferent species. Our analyses of multi-chemical releases utilized ~30 of the 36 detection bands. Figure 8 shows a recovered differential radiance spectrum from a simultaneous release of TCA (1000 ppmv) and n-butanol (2000 ppmv). The relative emission intensity attributed to each species is consistent with their relative concentrations in the plume and their known absorption coefficients.

We assessed our detection algorithm's susceptibility to interferent species by examining releases of DMMP, TCA, and n-butanol. The spectra of these species are not orthogonal as defined by Eq. (3). We assessed susceptibility to interferents by screening hyperspectral data sets for chemicals not included in the release and noting false positive detections. The images in Figure 9 illustrate this approach. The
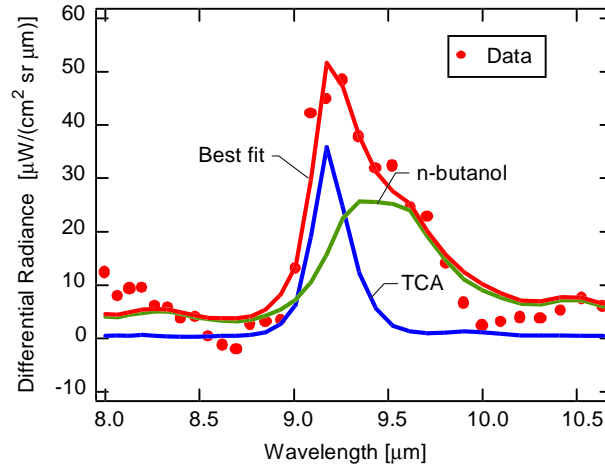
9

Figure 8. Recovered differential radiance spectrum from a pixel near the chimney orifice during a simultaneous TCA (1000 ppmv) and n-butanol (2000 ppmv) release (filled circles) along with the best fit reference spectra: TCA, n-butanol, and total emission.
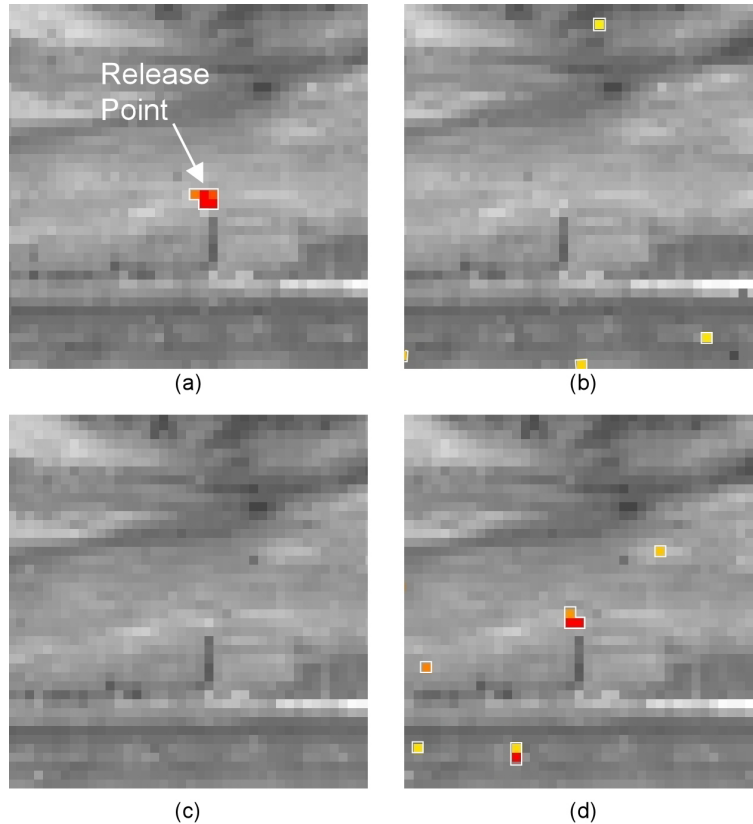

Figure 9. Upper left: highlighted pixels indicate high degree of correlation with TCA reference spectrum during TCA release; upper right: highlighted pixels indicate high degree of correlation with n-butanol reference spectrum during TCA release; highlighted pixels indicate high degree of correlation with TCA reference spectrum during n-butanol release; highlighted pixels indicate high degree of correlation with n-butanol reference spectrum during n-butanol release.

10

image in the upper left quadrant indicates the pixels testing positive for TCA during a TCA release. The image the lower left quadrant shows pixels testing positive for n-butanol during an n-butanol release. The images in the upper right and lower left quadrants show pixels testing positive for n-butanol during a TCA release and TCA during an n-butanol release, respectively. The false positive rate for n-butanol was low and false positives did not occur in the vicinity of the TCA release point. No false positives were observed when screening data cubes for the TCA spectrum. This appears to be because the n-butanol spectrum is less structured than the TCA spectrum. We have not yet developed a quantitatively predicting interference levels; however, qualitative assessment of our detection approach suggests that it is quite robust.

PASSIVE RANGING

During the 2001 field tests we used the 64 x 64 AIRIS and 256 x 256 AIRIS units in concert to demonstrate the ability to determine range-to-plume using only passive sensors. It was a simple tri-angulation measurement. The plume viewing geometry is illustrated in Figure 10. The distance between the sensors was determined using a handheld GPS unit with a measurement accuracy of ±0.01 km. The angles α and β were determined using the rotation stages on which each of the sensor heads was mounted. The angle α is determined by centering Sensor 2 in Sensor 1's field-of-regard, rotating the field-of-regard so that the plume release point is roughly centered, and noting the angle of rotation. The actual angle is calculated by adding angular shift of the detected plume relative to the center of the field-of-regard. (Each pixel's IFOV is known *a priori*, so calculating the angular shift is trivial.) The distance from Sensor 1 to the target is:

$$R_1 = \frac{L_s}{\cos\alpha}\left[\frac{\tan\alpha}{\tan\alpha + \tan\beta}\right] \qquad (4)$$

We calculate the uncertainty in the range to target as:

$$\delta R_1 = \sqrt{\left(\frac{dR_1}{dL_s}\right)^2 \delta L_s^2 + \left(\frac{dR_1}{d\alpha}\right)^2 \delta\alpha^2 + \left(\frac{dR_1}{d\beta}\right)^2 \delta\beta^2} \qquad (5)$$
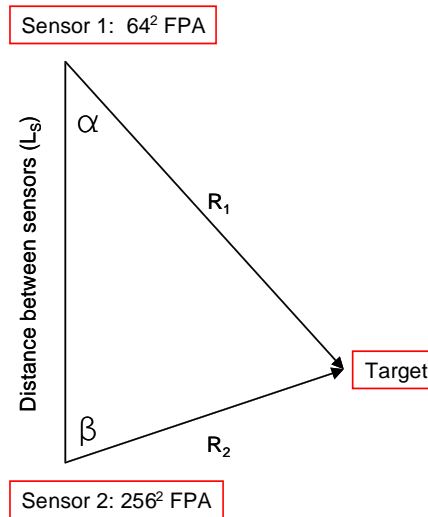

Figure 10. Viewing geometry for passive ranging of chemical vapor plumes.

11

where δX is the uncertainty in the quantity X. Table 3 lists calculated range-to-target and the uncertainties associated with the variables in the calculation. The uncertainty in α and β is determined by the backlash and slop in the sensor rotation stages. The listed values are the standard deviation of measurements made on multiple days. The calculated ranges are in excellent agreement with the GPS measurements.

TABLE 3. Passive Ranging: Calcuation Inputs and Results

Parameter	Value (Uncertainty[a])
R_1, calculated [km]	2.02(10)
R_1, actual [km]	1.90[b](1)
R_2, calculated [km]	1.64(10)
R_2, actual [km]	1.53[b](1)
L_s [km]	0.90[b](1)
α [deg]	53(1)
β [deg]	102(1)

a. uncertainty is in the last digit(s)
b. R_1, R_2, and L_s were measured by handheld GPS to ±0.01 km.

CONCLUSIONS

We have demonstrated that *AIRIS*, PSI's LWIR imaging Fabry-Perot spectrometer, functions effectively as a chemical imaging sensor. The instrument enables selective detection chemical species in vapor plumes containing one or multiple species. Our detection approach appears exhibits a low false positive detection rate, ~10^{-4}, while detecting chemical plumes at levels equivalent to OD=0.1 against $\Delta T = 6$ K. Our capability to detect and visualize vapor plumes is limited by the spectral clutter in the background scene, ~3 μW/(cm^2 sr μm). Predictions of plume spectral radiance as function of distance downwind from the release point were made by coupling a modified Gaussian plume dispersion model with a multi-layer radiative transfer model. The model was exercised using data from sensors located in the plume release chimney as well as a nearby meteorologic station which recorded local atmospheric conditions. The predictions of the plume radiance model are in good agreement with the data.

Data obtained during the 2001 field tests is consistent with prior results[1] which demonstrated that effective detection of known target species does not require acquisition of every spectral resolution element over the spectrometer's operating range. By operating with a reduced number of detection bands, the *AIRIS* can, in principle, acquire data more rapidly than spectrometers which acquire full spectra, such as FTIR-based instruments. Reduced data sets may also be processed more rapidly than full data sets. These capabilities would allow AIRIS to survey larger areas for target chemicals over a shorter period of time. Passive ranging capability was also demonstrated at the 2001 field tests. The calculated ranges to the plume agreed with GPS measurements to within 6%.

ACKNOWLEDGMENTS

REFERENCES

1. Gittins, C.M., et al. Remote Sensing and Selective Detection of Chemical Vapor Plumes by LWIR Imaging Fabry-Perot Spectrometry. in Proceedings of the International Symposium on Spectral Sensing Research. 2001. Quebec City, Canada (in press).

2. Marinelli, W.J., et al., Tunable Fabry-Perot etalon-based long-wavelength infrared imaging spectroradiometer. Applied Optics, 1999. 38(12): p. 2594-2604.

3. Gittins, C.M., W.G. Lawrence, and W.J. Marinelli, Frequency-agile bandpass filter for direct detection lidar receivers. Applied Optics, 1998. 37: p. 8327-8335.

4. Theriault, J.-M., private communication, 2001.

5. Seinfeld, J.H., Air Pollution: Physical and Chemical Fundamentals. 1975, New York, NY: McGraw-Hill.

6. Flanigan, D.F., Prediction of the limits of detection of hazardous vapors by passive infrared with the use of MODTRAN. Applied Optics, 1996. 35(30): p. 6090-6098.